

PAPER

Numerical simulation of laser ablation of molybdenum target for laser-induced breakdown spectroscopic application

To cite this article: Cailong FU *et al* 2018 *Plasma Sci. Technol.* **20** 085501

View the [article online](#) for updates and enhancements.

Related content

- [Modeling of nanosecond pulsed laser processing of polymers in air and water](#)
Deepak Marla, Yang Zhang, Jesper H Hattel *et al.*
- [Spectroscopic characterization of laser ablated silicon plasma](#)
Hira Shakeel, M Mumtaz, S Shahzada *et al.*
- [Temporal and spatial dynamics of optical emission from laser ablation of the first wall materials of fusion device](#)
Dongye ZHAO, Cong LI, Yong WANG *et al.*

Numerical simulation of laser ablation of molybdenum target for laser-induced breakdown spectroscopic application

Cailong FU (付彩龙), Qi WANG (王奇) and Hongbin DING (丁洪斌)

School of Physics, Key Laboratory of Materials Modification by Laser, Ion and Electron Beams (Ministry of Education), Dalian University of Technology, Dalian 116024, People's Republic of China

E-mail: hding@dlut.edu.cn

Received 6 February 2018, revised 9 March 2018

Accepted for publication 13 March 2018

Published 6 July 2018



CrossMark

Abstract

Laser-induced breakdown spectroscopy has been recognized as a significant tool for element diagnostics in plasma–wall interaction. In this work, a one-dimensional numerical model is developed to simulate the laser ablation processes of a molybdenum (Mo) target in vacuum conditions. The thermal process of the interaction between the ns-pulse laser with wavelength of 1064 nm and the Mo target is described by the heat conduction equation. The plasma plume generation and expansion are described by Euler equations, in which the conservation of mass density, momentum and energy are included. Saha equations are used to describe the local thermal equilibrium of electrons, Mo atoms, Mo^+ and Mo^{2+} . Plasma shielding and emission are all considered in this model. The mainly numerical results are divided into three parts, as listed below. Firstly, the rule of the plasma shielding effect varying with laser intensity is demonstrated quantitatively and fitted with the Nelder function. Secondly, the key parameters of plasma plume, such as the number density of species, the propagation velocity and the temperature, are all calculated in this model. The results indicate that the propagation velocity of the plume center increased with time in a general trend, however, one valley value appeared at about 20 ns due to the pressure gradient near the target surface leading to negative plasma velocity. Thirdly, the persistent lines of a Mo atom in the wavelength range from 300 nm to 600 nm are selected and the spectrum is calculated. Moreover, the temporal evolutions of Mo's spectral lines at wavelength of 550.6494 nm, 553.3031 nm and 557.0444 nm are given and the results are compared with experimental data in this work.

Keywords: LIBS, ablation process, molybdenum target, numerical simulation

(Some figures may appear in colour only in the online journal)

1. Introduction

Nuclear fusion is one of the best ways for solving energy problems due to utility deuterium as a fuel, which is very abundant and clean. Plasma magnetic confinement fusion is a major approach to realizing fusion energy. However the plasma is hard to confine perfectly by a magnetic field, even for devices like the Experimental Advanced Superconducting Tokamak (EAST). This leads to series processes of plasma–wall interaction. The first walls of the tokamak devices are subjected to kinds of particle and energy fluxes [1, 2]. In addition, they are

bombarded by electromagnetic radiation and neutrons are created in the plasma. Because of the interactions between the edge plasma and the first walls, the wall materials are subjected to harmful mechanisms, such as erosion, re-deposition and fuel retention [3–8]. As a results, the performance of the system is affected and safety issues are raised, therefore control of steady-state and transient wall power loads to technically acceptable limits and the control of the in-vessel tritium inventory are required. On the other hand, the material of the first wall is significant for present and for future fusion devices due to the harsh conditions in tokamaks.

Since the 1960s [9], laser-induced breakdown spectroscopy (LIBS) has become a significant tool for component identification on various kinds of samples like metals, alloys [10–15]. It has been developed as an analysis technique for the first wall and the region near the diverter in fusion devices such as EAST due to the lower cost, little damage, and no need for pre-treatment [15–19]. Recently, most corresponding studies were carried out by experimental techniques [12, 20, 21]. However, the internal mechanisms involved in LIBS are so complicated that they cannot be explained clearly only by experiment. In a numerical model, several mechanisms for mass removal would be included, such as evaporation, thermal ablation, liquid ejection, phase explosion, and so on. Therefore, it would be necessary to develop one self-consistent numerical model for LIBS by which the experimental results could be analyzed accurately. It would be of benefit to understand the mechanisms and parameter effects on designing and developing the measurements based on LIBS.

Laser ablation is one of the most important issues in LIBS and is also used in numerous applications, such as pulsed-laser film deposition [22], nanoparticle manufacturing [23], chemical analysis [24], surgery [25], and so on. Over the past five decades, many scientists have attempted to model the laser ablation processes in different regimes of wavelength (1064 nm, 532 nm, and 266 nm), laser irradiance, pulse length (fs, ps, and ns), gas environment (vacuum, ambient gas) and target material [26–32]. Even so, the physical mechanisms involved still could not be understood clearly.

Because of its hardness and high melting point (ITER-like material), molybdenum (Mo) has been used as the wall material of EAST in recent years. The *in situ* LIBS diagnosis system in EAST has been developed to investigate the spatial distribution of plasma facing materials (PFMs) [33]. The spatial distribution of H/D atoms on the PFMs was studied to optimize the signal to background ratio for the *in situ* LIBS diagnosis. The developed LIBS approach has been applied to monitor D-retention and the cleaning performance (Li/D co-deposition) of the first wall (Mo) in the fusion device of EAST [13, 34].

However, there are no relative numeric simulation results to better explain experimental data. Therefore, the knowledge of the ablation processes such as laser heating, plasma plume generation, expansion, and the plasma emission is necessary to design an approach for better diagnostics. Considering those factors, the *in situ* LIBS diagnostics of first wall is crucial.

In this work, a one-dimensional gas-dynamic numeric model is developed to simulate the laser ablation processes of Mo material in vacuum condition similar to the running conditions in EAST. The thermal process of the interaction between the ns-pulse laser with wavelength of 1064 nm and the Mo target is described by the heat conduction equation. The plasma plume generation and expansion are described by Euler equations, in which the conservation of mass density, momentum and energy are included. Moreover, Saha equations are used to describe the local thermal equilibrium (LTE) of

electrons, Mo atoms, Mo⁺, and Mo²⁺. Plasma shielding and optical emission were all considered in this model. The mainly numeric results are given and compared with experimental data in the paper.

2. Theory

To simulate the ablation processes between the nanosecond (ns) laser and the Mo target in vacuum conditions, four main processes are included in the present numeric model:

- (1) laser heating and phase change of the target material,
- (2) vapor production and plasma plume expansion,
- (3) plasma shielding,
- (4) plasma spectral radiation.

For the interaction between the ns laser pulse and metal target, the electromagnetic energy from laser light is converted into heat and a local thermodynamic equilibrium state is established. The temporal and spatial evolutions of the temperature inside the target are described by the heat conduction equation [35–37]:

$$c_p \rho \left[\frac{\partial T_s(t, x)}{\partial t} - u_{\text{rec}}(t) \frac{\partial T_s(t, x)}{\partial x} \right] = \frac{\partial}{\partial x} \left(k \frac{\partial T_s(t, x)}{\partial x} \right) + (1 - R_f) \alpha I(t) \exp(-\alpha x) \quad (1)$$

where T_s , c_p , ρ , k , and $u_{\text{rec}}(t)$ represent temperature, specific heat, mass density, thermal conductivity and the rate of surface recession, respectively, and x is the depth inside the target from the surface ($x = 0$). R_f is the surface reflectivity, which depends on the laser fluence as well as the target material. $I(t)$ is the laser intensity at the surface assumed to have a temporal Gaussian distribution.

The boundary conditions at the target surface for equation (1) is

$$(1 - R_f)I(t) = -k \frac{\partial T_s(t, x)}{\partial x} \Big|_{x=0} + \rho(t) u_{\text{rec}}(t) \Delta H_{\text{vap}} \quad (2)$$

where ΔH_{vap} is the heat of vaporization. Expansion of the plume is governed by the time dependent Euler equations with format [38]:

$$U_t + F(U)_x = S(U), \quad U = \begin{bmatrix} \rho \\ \rho v \\ E \end{bmatrix}, \quad F = \begin{bmatrix} \rho v \\ \rho v^2 + p \\ v(E + p) \end{bmatrix}, \quad (3)$$

$$S = \begin{bmatrix} 0 \\ 0 \\ a_{\text{IB}} I_{\text{laser}} - \varepsilon_{\text{rad}} \end{bmatrix}$$

where ρ is the vapor density, v is the propagating velocity of the vapor stream, E is the total energy and p is pressure. For the source term of energy, both the absorption of laser beam energy through the inverse Bremsstrahlung of electrons in the fields of neutrals and ions ($a_{\text{IB}} I_{\text{laser}}$) and the loss due to the Bremsstrahlung process (ε_{rad}) are considered. The caloric equation of state is applied to close the Euler equations, and

the total energy is calculated by the summation of kinetic, internal and ionizations energies [38]:

$$E = \frac{1}{2}\rho u^2 + \frac{P}{(\gamma - 1)} + IP_1 \frac{\rho x_+}{M_{\text{Mo}}} + (IP_1 + IP_2) \frac{\rho x_{2+}}{M_{\text{Mo}}} + \dots, \quad (4)$$

where γ is the ratio of specific heat, IP_1 and IP_2 are the first and the second ionization potentials, M_{Mo} is the molar mass of Mo, and x_+ and x_{2+} are the fraction of Mo^+ and Mo^{2+} , respectively. a_{IB} in equation (3) is given by summation of the electron-neutral and electron-ion inverse Bremsstrahlung absorption coefficients [27]:

$$\alpha_{\text{IB,e-n}} = \left[1 - \exp\left(-\frac{hc}{\lambda k_{\text{B}}T}\right) \right] \frac{\rho^2}{m_{\text{Mo}}^2} Q x_e x_0 \quad (5)$$

$$\alpha_{\text{IB,e-i}} = \left[1 - \exp\left(-\frac{hc}{\lambda k_{\text{B}}T}\right) \right] \frac{4e'^6 \lambda^3 x_e}{3hc^4 m_e} \left(\frac{2\pi}{3m_e kT} \right)^{1/2} \times \frac{\rho^2}{m_{\text{Mo}}^2} (x_+ + 4x_{2+}) \quad (6)$$

where Q is the cross section for photon absorption by electrons during the collision with neutrals, λ is the laser wavelength, $e' = e/\sqrt{4\pi\epsilon_0}$, m_e and e are the mass and charge of an electron, ϵ_0 , k_{B} , c and h are the vacuum permittivity, Boltzmann constant, velocity of light and Planck constant, respectively. m_{Mo} is the mass of one Mo atom and x_e , x_0 , x_+ and x_{2+} are the fractions of electrons, neutrals and ions, respectively.

Conversely, the loss of energy (ϵ_{rad}) occurs in plasma before and after pulse duration due to the Bremsstrahlung process [27]:

$$\epsilon_{\text{rad}} = \left(\frac{2\pi k_{\text{B}}T}{3m_e} \right)^{1/2} \frac{32\pi e'^6}{3hm_e c^3} \frac{\rho^2}{m_{\text{Mo}}^2} x_e (x_+ + 4x_{2+}). \quad (7)$$

Temperature is related to the partial pressures of vapor and electrons using the ideal gas law [38]:

$$T = \frac{m_{\text{Mo}} P}{(1 + x_e) k_{\text{B}} \rho}. \quad (8)$$

Furthermore, the electron and ions fractions can be calculated by the Saha equations (equations (9), (10)) in combination with the conservation of matter (equation (11)) and charge (equation (12)) as the local thermal equilibrium is assumed [27]:

$$\frac{x_+ x_e}{x_0} = \frac{m_{\text{Mo}}}{\rho} \left(\frac{2\pi m_e k_{\text{B}}T}{h^2} \right)^{3/2} e^{\left(-\frac{IP_1}{k_{\text{B}}T}\right)} \quad (9)$$

$$\frac{x_{2+} x_e}{x_+} = \frac{m_{\text{Mo}}}{\rho} \left(\frac{2\pi m_e k_{\text{B}}T}{h^2} \right)^{3/2} e^{\left(-\frac{IP_2}{k_{\text{B}}T}\right)} \quad (10)$$

$$x_0 + x_+ + x_{2+} = 1 \quad (11)$$

$$x_+ + 2x_{2+} = x_e. \quad (12)$$

Plasma optical emission consists of background emission, atomic, molecular, and ionic spectral lines as well as continuous radiation. Because of the Bremsstrahlung, continuous radiation happens near the target surface at the initial stage. Then, plasma cools down, electrons recombine with the ions, and spectral lines appear. Line emission is calculated by the summation of sample lines [28]:

$$I_{\text{line}}(v_i) = \sum_j^{N_s} L_j(v_i, v_j, \gamma_{ul}^j) E_{\text{line}}^j(v_j) \quad (14)$$

where $L_j(v_i, v_j, \gamma_{ul}^j)$ is the profile of the j th spectral line, $E_{\text{line}}^j(v_j)$ is the peak value of j th line, and N_s is the number of selected strong lines.

In the model, the Stark effect is the main mechanism of line broadening since a large number of electrons and ions exist in plasma at an initial period of laser irradiation. Due to the Stark broadening of each line, the Lorentz line profile can be calculated by [28]:

$$L_j(v_i, v_j, \gamma_{ul}^j) = \frac{(\gamma_{ul}^j/4\pi^2)}{(v_i - v_j)^2 + (\gamma_{ul}^j/4\pi)^2} \quad (15)$$

where γ_{ul}^j is the decay rate and depends on the Stark line width, and v_i and v_j are the frequency of i th and j th strong lines, respectively [28].

$$\gamma_{ul}^j = 2\pi(c/\lambda^2)\Delta\lambda_{\text{stark}}^j \quad (16)$$

where c is the light speed and the FWHM width of the j th line in the spectral lines can be calculated by [39]:

$$\Delta\lambda_{\text{stark}}^j = \frac{2\omega n_e}{n_{\text{ref}}} \quad (17)$$

where ω is the Stark or electron impact parameter, n_e is the number density of the electrons and n_{ref} is the related number density [28].

3. Results and discussion

The simulation parameters are chosen as follows: the laser pulse is set to 5 ns, and the amplitude of laser irradiance intensity ranges from $9 \times 10^{11} \text{ W m}^{-2}$ to $1 \times 10^{14} \text{ W m}^{-2}$.

The selected strong lines of Mo are listed in table 1.

When the laser irradiance is set to $9 \times 10^{12} \text{ W m}^{-2}$, the calculated laser intensity profile on the surface of the target varied with time, as shown in figure 1. The red line represents the original laser pulse and the black one is the real intensity of the laser irradiance on the target after plasma shielding. It is obvious that the plasma shielding effect can be observed. In order to describe the effect of the plasma shielding quantitatively, we calculate the percentage of the laser energy going through the plasma. It is found that the value is 32% in this case.

Figure 2 describes the percentage of the plasma shielding effect varying with the laser irradiance from $9 \times 10^{11} \text{ W m}^{-2}$ to $1 \times 10^{14} \text{ W m}^{-2}$. It is obvious that higher laser irradiance leads to lower laser penetration rate. The percentage value is 100% at the lowest laser irradiance of $9 \times 10^{11} \text{ W m}^{-2}$,

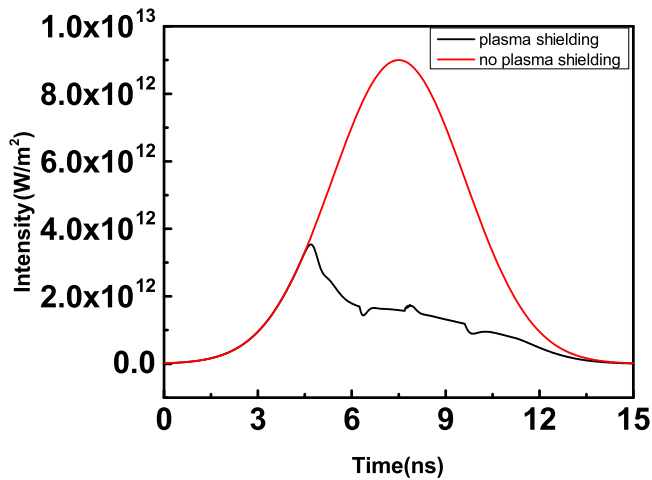


Figure 1. Temporal distributions of the laser intensity profile on the surface of the Mo target without laser-produced plasma (red curve) and with laser plasma shielding (black curve).

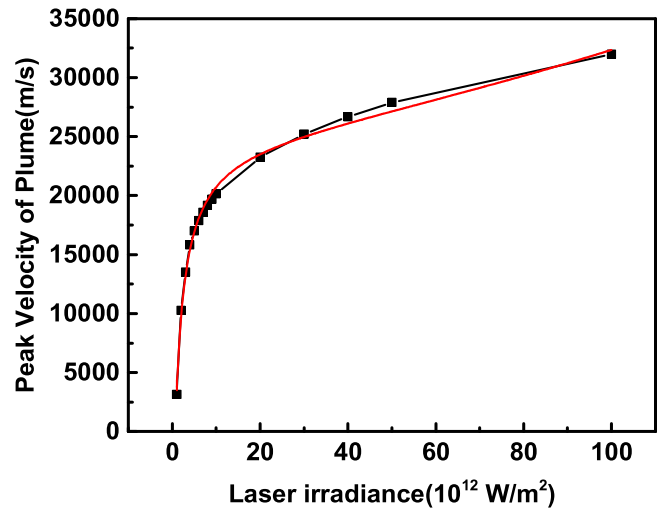


Figure 3. The velocity of the plasma plume front as a function of laser irradiance at a delay time of 100 ns.

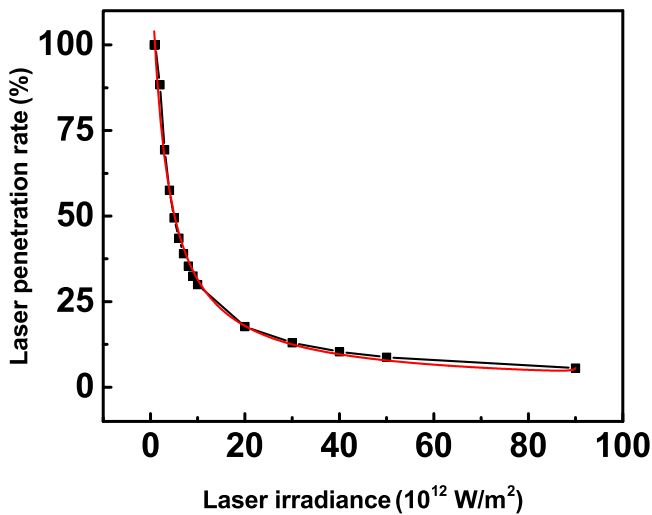


Figure 2. Laser penetration rate: a function of laser irradiance at the delay time of 100 ns.

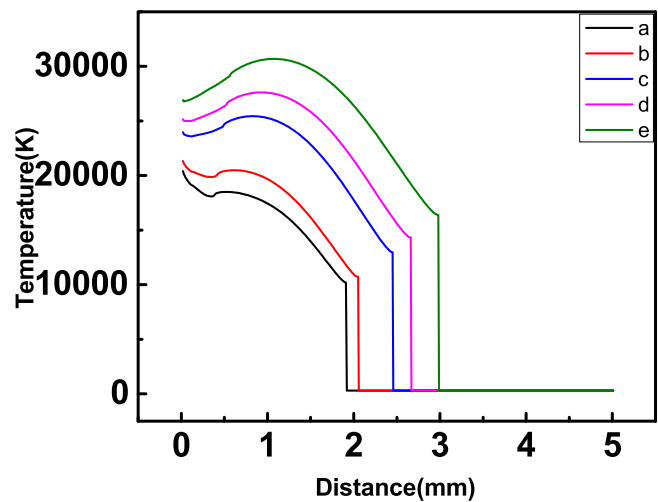


Figure 4. Plasma temperature distributions at 100 ns in the different laser irradiances: (a) $7 \times 10^{12} \text{ W m}^{-2}$, (b) $1 \times 10^{13} \text{ W m}^{-2}$, (c) $3 \times 10^{13} \text{ W m}^{-2}$, (d) $5 \times 10^{13} \text{ W m}^{-2}$, (e) $1 \times 10^{14} \text{ W m}^{-2}$.

Table 1. Persistent lines of neutral Mo from NIST.

Wavelength (nm)	Einstein coefficient $A \times 10^8 \text{ (s}^{-1}\text{)}$	Energy of upper level (eV)	Degeneracy
313.2594	1.79	3.956 7289	9
315.8166	0.463	3.924 6932	7
317.0343	1.37	3.909 6192	7
319.3978	1.53	3.880 6900	5
320.8838	0.277	3.862 7196	5
344.7123	0.88	5.126 4569	11
379.8252	0.69	3.263 3161	9
386.4103	0.624	3.207 7051	7
390.2953	0.617	3.175 7767	5
406.9881	0.352	5.126 4569	11
418.8323	0.33	5.040 4165	13
550.6493	0.361	3.586 0778	7
553.3031	0.372	3.575 2817	5
557.0444	0.33	3.560 2362	3

which means an obvious plasma shielding effect cannot be seen and the laser energy can reach the target surface easily with little loss. The penetration decreases sharply at the initial stage and then it decreases slowly after laser irradiance $> 10 \times 10^{12} \text{ W m}^{-2}$. The percentage is almost 0% as the laser irradiance is more than $90 \times 10^{12} \text{ W m}^{-2}$. The calculations indicate that the plasma absorbs more laser energy and the shielding effect is more and more significant as the laser irradiance increases. As shown in figure 2, the curve fits well with the Nelder function $y = (x + a)/(b_0 + b_1*(x + a) + b_2*(x + a)^2)$, where the values of a , b_0 , b_1 and b_2 are -90.96 , 0.044 , 0.22 and 0.0024 , respectively.

The velocity of the plasma plume front with different laser irradiance at 100 ns is shown in figure 3. When the laser irradiance is set to $1 \times 10^{12} \text{ W m}^{-2}$, the plume velocity is 3200 m s^{-1} , as can be seen from the left point. Then the velocity increases abruptly to 20000 m s^{-1} when the laser

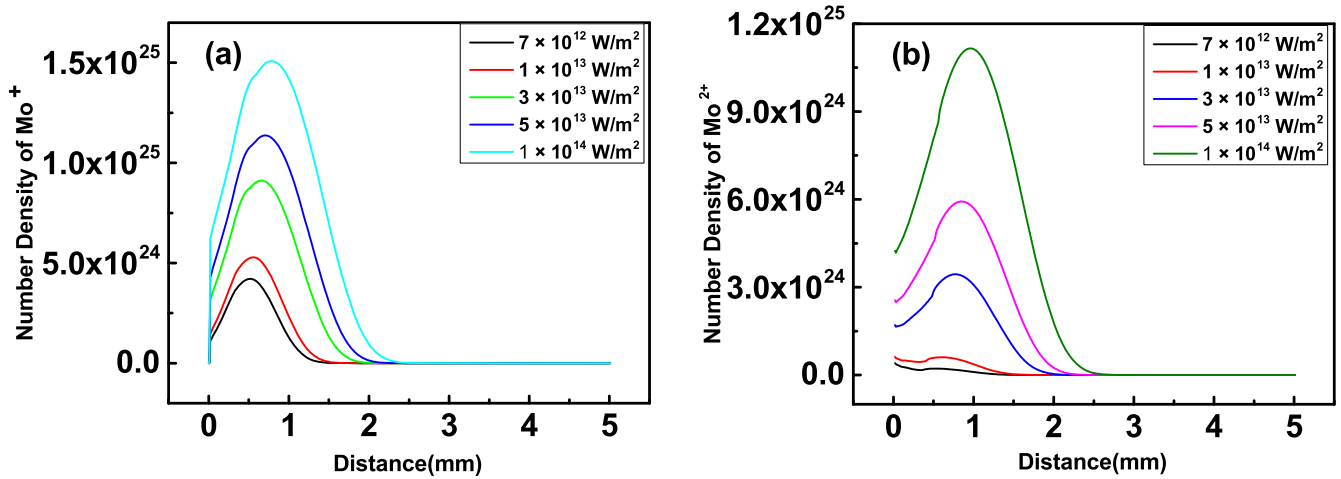


Figure 5. Spatial distribution of number density for the ions (a) Mo^+ and (b) Mo^{2+} at 100 ns at the different laser irradiances: $7 \times 10^{12} W m^{-2}$, $1 \times 10^{13} W m^{-2}$, $3 \times 10^{13} W m^{-2}$, $5 \times 10^{13} W m^{-2}$ and $1 \times 10^{14} W m^{-2}$.

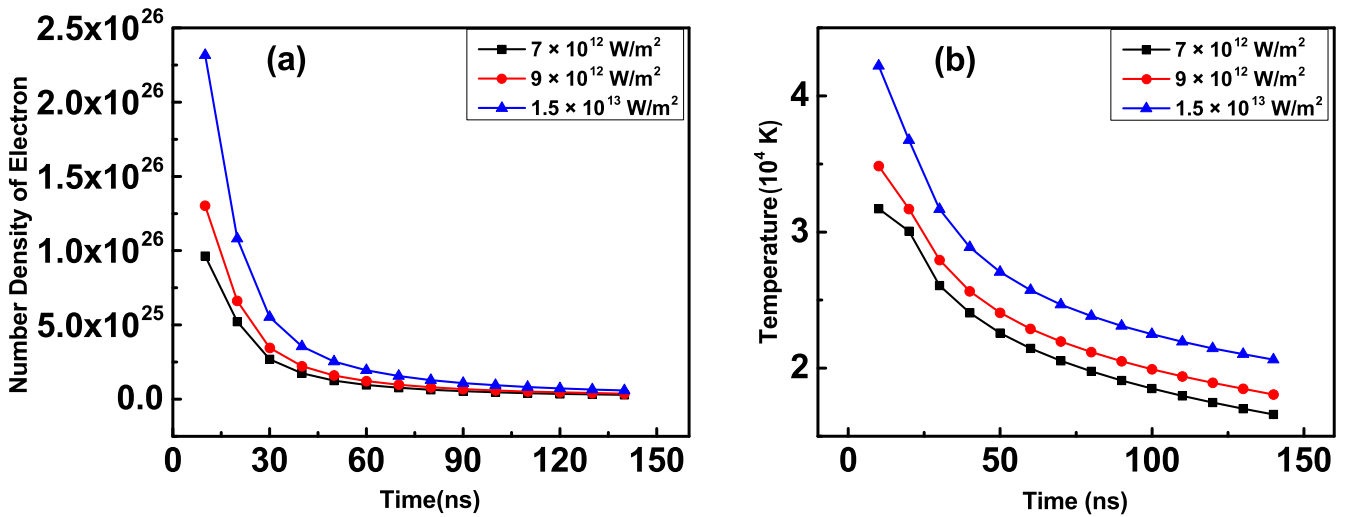


Figure 6. Temporal evolution of the plasma density and plasma temperature in the different laser irradiances: (a) electron number density in the plasma plume center and (b) electron temperature in the plasma plume center.

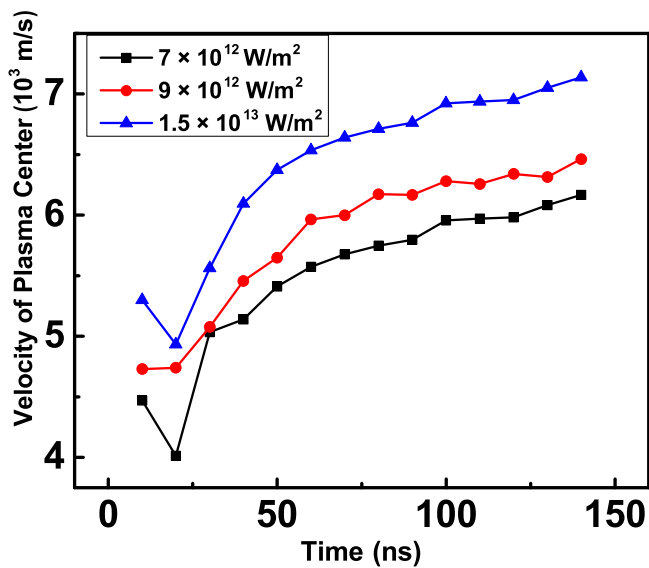


Figure 7. Velocity of the plasma plume center as a function of time at the different laser irradiances.

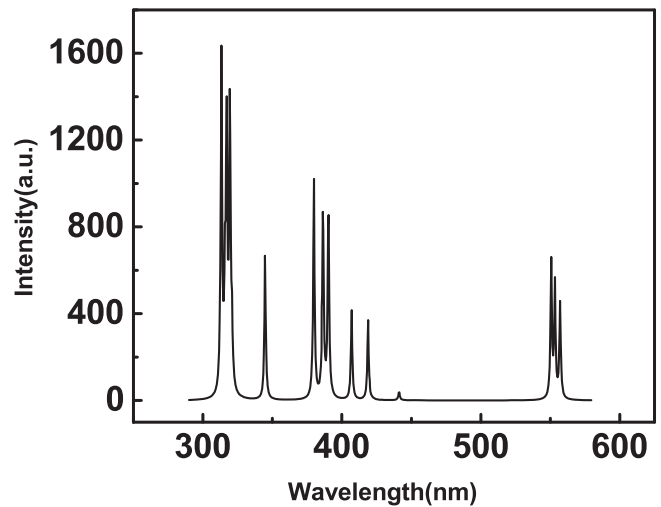


Figure 8. The calculated spectrum from the laser ablation Mo target in the region from 280 nm to 580 nm.

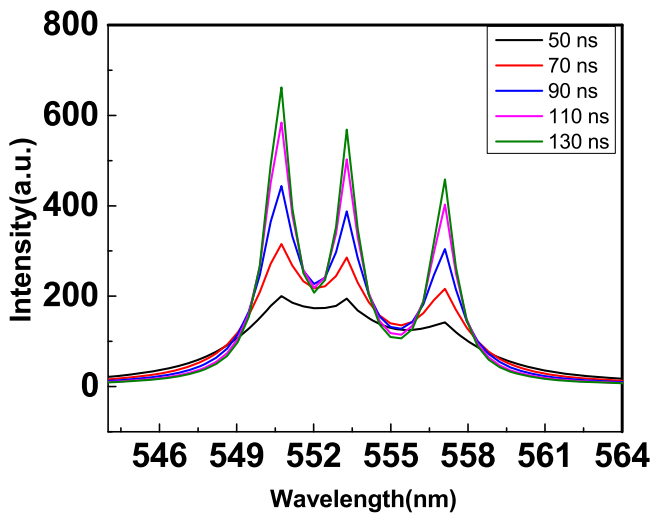


Figure 9. The profiles of Mo spectral lines in the region from 545 nm to 564 nm at different times in laser irradiance of $5 \times 10^{13} \text{ W m}^{-2}$.

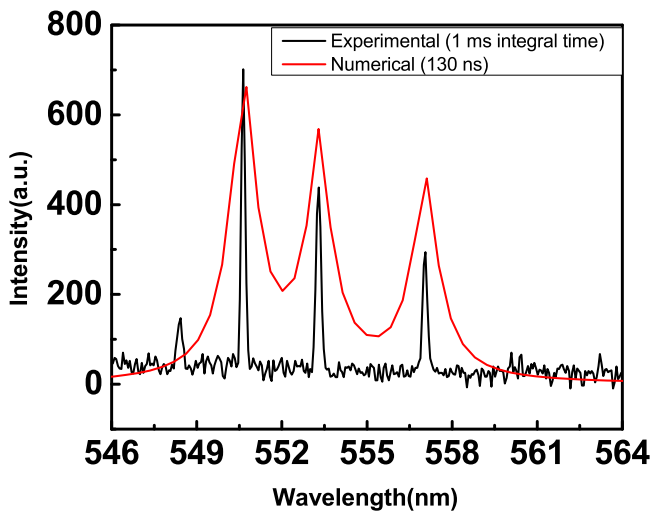


Figure 10. The calculated (red line) and experimental (black line) spectral lines of the Mo target in the wavelength region from 545 nm to 564 nm.

irradiance increases to $1 \times 10^{13} \text{ W m}^{-2}$. Eventually, the trend turns to almost linear increase after the irradiance of $9 \times 10^{12} \text{ W m}^{-2}$. It is found that this curve can also be fitted well with the Nelder function $y = (x + a) / (b_0 + b_1(x + a) + b_2(x + a)^2)$, where the values of a , b_0 , b_1 and b_2 are -6.5355 , 8.45116×10^{-5} , 4.01538×10^{-5} and -1.01537×10^{-7} , respectively.

In figure 4, the maximum temperature is about 20 000 K for laser irradiance of $7 \times 10^{12} \text{ W m}^{-2}$, 22 000 K for laser irradiance of $10 \times 10^{12} \text{ W m}^{-2}$, 25 000 K for laser irradiance of $30 \times 10^{12} \text{ W m}^{-2}$, 27 500 K for laser irradiance of $50 \times 10^{12} \text{ W m}^{-2}$ and 31 000 K for laser irradiance of $100 \times 10^{12} \text{ W m}^{-2}$. The horizontal coordinate is the perpendicular distance from the measuring position to the target surface. It can be seen clearly that the lower the laser irradiance is, the shorter the plasma plume length. It can also

be found that the plasma temperature is influenced by laser irradiance, and the temperature of the plasma front is lower than that in the center region due to the plume expansion.

In figure 5, the horizontal coordinate is the perpendicular distance from the measuring position to the target surface. As time goes on, plasma moves backward to the target surface and the peak density of the plasma plume becomes lower due to plume expansion. It can be deduced from figure 5 that the number density of Mo^+ is higher than that of Mo^{2+} , and both of them increase along with the laser energy.

The temporal evolutions of the plasma density at different laser irradiance are given in figure 6(a). For the case $1.5 \times 10^{13} \text{ W m}^{-2}$, the peak value of the number density is $2.3 \times 10^{26} \text{ m}^{-3}$ at 10 ns. Then a sharp decrease happens before 50 ns since the laser pulse, which provides the heat source, sustains less than 20 ns (the full width at half maximum (FWHM) is 5 ns). The plasma constricts to the surface of the target and the plasma density decreases because the material evaporates due to high surface temperature. After 50 ns, the number density reduces gradually to $1.0 \times 10^{25} \text{ m}^{-3}$. Figure 6(b) demonstrates the temporal evolutions of the temperature for different laser irradiances of $7 \times 10^{12} \text{ W m}^{-2}$, $9 \times 10^{12} \text{ W m}^{-2}$, and $1.5 \times 10^{13} \text{ W m}^{-2}$ in times ranging from 10 ns to 140 ns. It is shown that the temperature decreases over time and the higher temperature corresponds to stronger laser irradiance.

In figure 7, the general trend of the velocity rises with the time increasing due to plasma plume adiabatic expansion while one valley appears at 20 ns, which is caused by the pressure gradient near the target surface resulting in negative plasma velocity. It also can be found that higher laser irradiance leads to faster plume expansion velocity.

Figure 8 shows the numerical results of spectral intensity in vacuum condition at 100 ns in laser irradiance of $7 \times 10^{12} \text{ W m}^{-2}$. Fourteen persistent lines are observed at wavelengths of 313.2594 nm, 315.8166 nm, 317.0343 nm, 319.3978 nm, 320.8838 nm, 344.7123 nm, 379.8252 nm, 386.4103 nm, 390.2953 nm, 406.9881 nm, 418.8323 nm, 550.6493 nm, 553.3031 nm and 557.0444 nm. As is shown, the intensity in the UV range is stronger than that in the visible range.

Figure 9 illustrates the numerical results of Mo spectra in the range of 545 nm to 564 nm at various delay times of 50 ns, 70 ns, 90 ns, 110 ns and 130 ns. Three peaks appear at the wavelengths of 550.6493 nm, 553.3031 nm and 557.0444 nm, respectively. It is shown that the strongest peak is at 550.6493 nm and the intensity increasing with time.

Figure 10 illustrates the comparison between numerical and experimental results of Mo lines in wavelength from 545 nm to 564 nm at laser irradiance of $7 \times 10^{12} \text{ W m}^{-2}$. The experimental spectrum of Mo lines with integral time is 1 ms. The numeric spectrum of Mo lines with 130 ns integral time. Due to the high density of electron, the Stark broadening effect dominates at 130 ns. So the calculated profiles of the spectral lines are wider than the experimental ones that were observed at a delay of 1 ms.

4. Conclusions

In this work, a one-dimensional numeric model was developed to simulate the laser ablation processes of Mo material in vacuum conditions similar to the running conditions in EAST. The thermal processes, heating, melting, vapor production and expansion, plasma formation and plasma shielding, and plasma emission were all considered in this model. The mainly numeric results were divided into three parts. Firstly, the rule of the plasma shielding effect as a function of irradiance was demonstrated quantitatively and fitted with the Nelder function. Secondly, the key parameters of the plasma plume such as the number density of species, the propagation velocity, and the temperature were all calculated in this model. Thirdly, the persistent lines of the Mo atom in the wavelength range from 300 nm to 600 nm were selected and the spectrum was calculated. Moreover, the temporal evolutions of Mo's spectral lines were given and the results were compared with experimental data.

Acknowledgments

This work was supported by National Magnetic Confinement Fusion Science Program of China (No. 2013GB109005), National Natural Science Foundation of China (Nos. 11475039, 11605023).

References

- [1] Rubel M, Wienhold P and Hildebrandt D 2001 *J. Nucl. Mater.* **290-293** 473
- [2] Wang L et al 2014 *Nucl. Fusion* **54** 114002
- [3] Philipps V et al 2013 *Nucl. Fusion* **53** 093002
- [4] Mercadier L et al 2011 *J. Nucl. Mater.* **414** 485
- [5] Gierse N et al 2011 *J. Nucl. Mater.* **415** S1195
- [6] Xiao Q et al 2013 *Fusion Eng. Des.* **88** 1813
- [7] Hai R et al 2013 *J. Nucl. Mater.* **436** 118
- [8] Coad J P et al 2001 *J. Nucl. Mater.* **290-293** 224
- [9] Brech F and Cross L 1962 *Appl. Spectrosc.* **16** 59
- [10] Caneve L et al 2006 *Appl. Phys. A* **85** 151
- [11] Wang Z et al 2014 *Front. Phys.* **9** 419
- [12] Farid N et al 2013 *J. Nucl. Mater.* **433** 80
- [13] Hai R et al 2013 *Spectrochim. Acta. Part B At. Spectrosc.* **87** 147
- [14] Hai R et al 2013 *J. Nucl. Mater.* **438** S1168
- [15] Farid N et al 2013 *J. Nucl. Mater.* **438** 183
- [16] Pandhija S et al 2010 *Appl. Phys. B* **98** 231
- [17] Schweer B et al 2009 *Phys. Scr.* **2009** 014008
- [18] Farid N et al 2014 *Nucl. Fusion* **54** 012002
- [19] Zhao D Y et al 2014 *Plasma Sci. Technol.* **16** 149
- [20] Farid N et al 2014 *J. Appl. Phys.* **115** 033107
- [21] Farid N et al 2013 *Appl. Phys. Lett.* **103** 191112
- [22] Vijayalakshmi S et al 1998 *Appl. Surf. Sci.* **127-129** 378
- [23] Becker M F et al 1998 *Nanostruct. Mater.* **10** 853
- [24] Winefordner J D et al 2000 *J. Anal. At. Spectrom.* **15** 1161
- [25] Loesel F H et al 1998 *Appl. Phys. B* **66** 121
- [26] Zhigilei L V, Lin Z B and Ivanov D S 2009 *J. Phys. Chem. C* **113** 11892
- [27] Bogaerts A et al 2003 *Spectrochim. Acta Part B At. Spectrosc.* **58** 1867
- [28] Rezaei F and Tavassoli S H 2012 *Spectrochim. Acta Part B At. Spectrosc.* **78** 29
- [29] Ivanov D S and Zhigilei L V 2003 *Phys. Rev. B* **68** 064114
- [30] Oderji H Y et al 2016 *Spectrochim. Acta Part B At. Spectrosc.* **122** 1
- [31] Stafe M 2012 *J. Appl. Phys.* **112** 123112
- [32] Aghaei M, Mehrabian S and Tavassoli S H 2008 *J. Appl. Phys.* **104** 053303
- [33] Li C et al 2015 *Plasma Sci. Technol.* **17** 638
- [34] Liu P et al 2017 *Fusion Eng. Des.* **118** 98
- [35] Svendsen W, Ellegaard O and Schou J 1996 *Appl. Phys. A* **63** 247
- [36] Bhattacharya D, Singh R K and Holloway P H 1991 *J. Appl. Phys.* **70** 5433
- [37] Ho J R, Grigoropoulos C P and Humphrey J A C 1995 *J. Appl. Phys.* **78** 4696
- [38] Balazs L, Gijbels R and Vertes A 1991 *Anal. Chem.* **63** 314
- [39] Alonso-Medina A 2008 *Spectrochim. Acta Part B At. Spectrosc.* **63** 598